

Maximizing bipolar sensitivity for anomalous Nernst thermopiles in heat flux sensing in amorphous GdCo alloys

Miho Odagiri, Hiroto Imaeda, Ahmet Yagmur, Yuichiro Kurokawa, Satoshi Sumi, Hiroyuki Awano, and Kenji Tanabe*

*tanabe@toyota-ti.ac.jp

Abstract

A Heat Flux Sensor (HFS) facilitates the visualization of heat flow, unlike a temperature sensor, and is anticipated to be a key technology in managing waste heat. Recently, an HFS utilizing the Anomalous Nernst Effect (ANE) has been proposed garnering significant interest in enhancing the transverse Seebeck coefficient. However, ideal materials for HFS not only require a large transverse Seebeck coefficient but also meet several criteria including low thermal conductivity and a bipolar nature of the transverse Seebeck coefficient, especially a negative coefficient. In this study, we have investigated ANE in amorphous ferrimagnetic GdCo alloys, revealing their numerous advantages as HFS materials. These include a large transverse Seebeck coefficient, extremely low thermal conductivity, large negative sensitivity, unparalleled bipolar sensitivity, versatility for deposition on various substrates, and a small longitudinal Seebeck coefficient. These qualities position GdCo films as promising candidates for the advancement of HFS technology.

Introduction

A Heat Flux Sensor (HFS) is pivotal in visualizing heat flow, a capability beyond the scope of standard temperature sensors, and is deemed essential in the management of waste heat. Traditional HFS systems, based on the Seebeck effect where the electromotive force is generated parallel to a temperature gradient, are notably expensive due to complex fabrication processes and the need for precise sensitivity calibration.

In a significant development, Zhou et al. have proposed an HFS design utilizing the Anomalous Nernst Effect (ANE). This approach generates an electromotive force perpendicular to the temperature gradient, presenting several advantages¹. The use of thin film technology in these ANE-based HFS devices promises ease of manufacturing, improved reproducibility, and the potential for a flexible sensor. The ANE is mathematically represented as:

$$\mathbf{E} = S_{\text{ANE}} \left(\frac{\mathbf{M}}{|\mathbf{M}|} \times (-\nabla T) \right), \quad (1)$$

where \mathbf{E} is an electric field induced by ANE, S_{ANE} is a transverse Seebeck coefficient, ∇T is the temperature gradient, and \mathbf{M} is magnetization. S_{ANE} is a critical factor in ANE research. Historically, the ANE has been studied as one of the transport properties from the viewpoint of fundamental physics since the Nernst effect had been discovered in 1887². A great turning point in ANE research is the studies by Sakuraba et al. from the viewpoint of applied physics^{1,3-4}. They proposed the application into the thermoelectric power source and HFS using a transverse thermopile structure in Fig. 1. After that many groups have reported the studies on the ANE at room temperature⁵⁻¹¹. Another breakthrough in ANE research was the discovery by Ikhlas et al. in 2017 of a relatively large S_{ANE} value of $0.6 \mu\text{VK}^{-1}$ in antiferromagnetic Mn_3Sn ¹². This finding was remarkable because the enhancement in S_{ANE} was attributed to the increased Berry curvature at Weyl points near the Fermi energy. This discovery spurred further research, with several groups identifying Weyl magnetic materials exhibiting even larger S_{ANE} values¹³⁻²⁷. For example, Sakai et al. and Guin et al. observed a giant ANE in the full-Heusler ferromagnet Co_2MnGa , achieving an S_{ANE} of $6 \mu\text{VK}^{-1}$ at room temperature^{13,14}.

The key parameter in evaluating an HFS is the ratio of thermal electromotive force (V) to the heat flux density (j), expressed as a sensor sensitivity V/j . This parameter is, however, a quantitative variable and depends on the sensor area and its shape. Hence, V/j is unsuitable as a parameter in evaluating materials. Instead of V/j , we use the ratio of electric field (E) induced by ANE to the heat flux density (j), expressed as E/j ,

to evaluate materials for ANE-based HFS. E/j is an intensifying variable and independent of the sensor area and its shape. According to Fourier's law and the definition of the transverse Seebeck coefficient (S_{ANE}), this ratio is given by:

$$\frac{E}{j} = \frac{S_{ANE}}{\kappa}, \quad (2)$$

where κ is the thermal conductivity. This equation underlines the necessity for materials with a large transverse Seebeck coefficient and low thermal conductivity for effective HFS design. When Zhou et al. proposed an innovative ANE-type HFS, they also demonstrated its viability using FeAl alloys¹. They showed that single-crystalline Fe₈₁Al₁₉ alloy films on MgO substrates and polycrystalline films on amorphous substrates both exhibit large S_{ANE} values (+3.4 and +3.1 μVK^{-1} , respectively), indicating that the sensitivity is largely independent of the substrate type. They fabricated an HFS that consists of the Fe₈₁Al₁₉-Au thermopile on a Si substrate and its sensor sensitivity V/j is +0.020 $\mu\text{VW}^{-1}\text{m}^2$ when the sensor area is $1 \times 1 \text{ cm}^2$. Note that the sensor sensitivity differs from the sensitivity for materials and depends on the sensor area and shape of the thermopile. From this sensor sensitivity, the material sensitivity E/j for these films is approximately estimated to be +0.20 μmA^{-1} . The unit of E/j is $(\text{Vm}^{-1})(\text{Wm}^{-2})^{-1}$ and it is simplified as mA^{-1} . Uchida et al. fabricated an HFS using a thermopile structure of Co₂MnGa and Au with a giant S_{ANE} of +6 μVK^{-1} at room temperature and its sensor sensitivity V/j is +0.110 $\mu\text{VW}^{-1}\text{m}^2$ under a magnetic field of 1 kOe²⁸. In contrast, the sensitivity at zero field reduces to +0.016 $\mu\text{VW}^{-1}\text{m}^2$ and they pointed out the importance of the remanent magnetization. Modak et al. focused on SmCo alloys, known for their high coercive force, and found that their sensitivity remains stable even at zero magnetic field²⁹. Tanaka et al. highlighted the importance of using two materials with similar longitudinal Seebeck coefficients (S_{xx}) to minimize the Seebeck effect's influence³⁰. The criteria for two materials of the HFS is not only large S_{ANE} , but also low thermal conductivity, bipolarity of S_{ANE} , similar small S_{xx} , and the flexibility to fabricate onto any substrates.

Rare-earth (RE) and transition-metal (TM) alloys, such as GdFeCo, are notable for their ferrimagnetic properties, characterized by the antiparallel alignment of the magnetic moments of TM and RE elements³¹⁻³⁴. These materials exhibit a diverse range of magnetic behaviors depending on their composition. In RE-rich films, the net magnetization aligns with the magnetic moment of the rare-earth metal, while in TM-rich films, the transition metal predominantly contributes to the net magnetization. The boundary composition between these RE-rich and TM-rich alloys is known as the magnetization compensation point (MCP). Additionally, the amorphous nature of these

alloys, arising from their lack of crystal structure, results in relatively low thermal conductivities. For instance, $\text{Gd}_{21}\text{Fe}_{72}\text{Co}_7$ and $\text{Tb}_{21}\text{Fe}_{73}\text{Co}_6$ films exhibit thermal conductivities of approximately 5.5 and $4.6 \text{ Wm}^{-1}\text{K}^{-1}$, respectively, at room temperature³⁵. The amorphous nature is advantageous for various practical applications, as it enables the deposition of these alloys on a wide range of substrates at room temperature. The unique combination of properties of RE-TM alloys, including their magnetic behavior, low thermal conductivity, and flexible deposition, make them valuable for practical use. Notably, they have already found applications in commercial magneto-optical storage systems, demonstrating their utility and versatility in advanced technological applications.

Several groups have reported the ANE in RE-TM alloys^{7,10,31,33,36-39}. Seki et al. explored the anomalous Ettingshausen effect, a counterpart to the ANE, in GdCo alloys and estimated the transverse Seebeck coefficient to be $0.18 \mu\text{VK}^{-1}$ in $\text{Gd}_{22}\text{Co}_{78}$ ³⁶. Liu et al. studied the ANE in $\text{Gd}_{16}\text{Co}_{84}$ and $\text{Gd}_{26}\text{Co}_{74}$ alloys³⁷, discovering that the polarity of the ANE signal is dictated by the magnetization orientation of the Co sub-lattices rather than the overall net magnetization of GdCo. Odagiri et al. studied the composition dependence of the ANE in TbCo alloys and discovered the coexistence of a large transverse Seebeck coefficient of nearly $1.0 \mu\text{VK}^{-1}$ and a large coercive force of more than 1 kOe ³⁹. However, the material sensitivity for an ANE-based HFS has never been investigated in the RE-TM alloys yet.

In this study, we present a comprehensive analysis of the composition dependence of the ANE in GdCo alloy films. We found that doping Gd into GdCo alloys substantially enhances the sensitivity (E/j), achieving a value of $0.23 \mu\text{mA}^{-1}$ near the MCP which is comparable to Co_2MnGa . The origin of high sensitivity is the relatively large S_{ANE} and extremely small κ . Moreover, GdCo exhibits bipolarity of the sensitivity E/j . This study, therefore, highlights the potential of GdCo alloys in advancing technologies that leverage the ANE.

Results and Discussion

Anomalous Nernst effect

The transverse Seebeck coefficient, S_{ANE} , was measured under conditions of a perpendicular magnetic field and an in-plane thermal gradient using the Hall bar samples as shown in Figs. 2(a-b). In Fig. 2(c), we plot the detected voltage as a function of an external magnetic field under the application of a constant thermal gradient for a GdCo sample with $x = 15.5$ at room temperature. The ANE voltage V is defined as half the voltage difference at high magnetic fields between positive and negative saturations.

We observe that V increases with a rising temperature difference. The absence of a hysteresis curve in this plot suggests that the sample possesses in-plane magnetic anisotropy. Figure 2(d) illustrates the ANE electric field E as a function of the temperature gradient ∇T , derived from the data in Fig. 2(c). E shows a direct proportionality to ∇T . The blue dotted line represents a linear fitting, and its slope corresponds to the transverse Seebeck coefficient S_{ANE} .

Figure 2(e) illustrates the composition-dependent behavior of S_{ANE} in GdCo films. The behavior is perfectly consistent with TbCo results³⁹, suggesting that the characteristics of S_{ANE} are related not to an orbital momentum in 4f electron of rare earth elements but to random Co position in the amorphous alloy. A notable change in the sign of S_{ANE} is observed between compositions $x = 15.5$ and 21.7 , corresponding to the change from a TM-rich to an RE-rich alloy composition. It means that ANE in GdCo is predominantly influenced by the Co moment. Unlike other materials with large S_{ANE} values such as $\text{Fe}_{81}\text{Al}_{19}$ ¹, which exhibit positive polarity, RE-rich GdCo alloys demonstrate significant negative polarity. This characteristic is crucial for applications requiring both positive and negative S_{ANE} values, such as a HFS. Additionally, the magnitude of S_{ANE} near the MCP remains relatively stable, around $1.0 \mu\text{VK}^{-1}$. The presence of a large S_{ANE} around the MCP, coupled with the sign change at the MCP, is vital for the development of HFS modules. The observed large $|S_{ANE}|$ of around $1.0 \mu\text{VK}^{-1}$ is inconsistent with the previous reports by Seki et al. and Liu et al. They used multilayer structures like $\text{Al}(4 \text{ nm})/\text{GdCo}(30 \text{ nm})/\text{Al}(4 \text{ nm})$ and $\text{Ta}(3 \text{ nm})/\text{GdCo}(4.7, 6.2 \text{ nm})/\text{Pt}(3 \text{ nm})/\text{Ta}(1 \text{ nm})$, potentially leading to an underestimation of $|S_{ANE}|$ due to the shunting effect of the metallic layers.

In the specific case of $x = 21.7$, close to the MCP, the decrease in the magnitude of S_{ANE} , reminiscent of the decrease observed in $\text{Tb}_{19.9}\text{Co}_{80.1}$ ³⁹, is observed in Fig. 2(e). This decrease originates from the coexistence of TM-rich and RE-rich regions like $\text{Tb}_{19.9}\text{Co}_{80.1}$.

Thermo-electric transport properties

We investigated the composition dependencies of electrical resistivity ρ_{xx} , Hall resistivity ρ_{yx} , and longitudinal Seebeck coefficient S_{xx} in GdCo alloys to elucidate the factors contributing to the observed large S_{ANE} values. Figures 3(a-c) show the schematic diagram of the measurement setup for ρ_{xx} , ρ_{yx} , and S_{xx} , and Figures 3(d-f) shows ρ_{xx} , ρ_{yx} , and S_{xx} as a function of the GdCo composition. As depicted in Fig. 3(f), S_{xx} decreases with increased Gd doping and becomes notably small around the MCP. According to the theories on thermo-electric transport properties, S_{ANE} can be

decomposed into two distinct contributions,

$$S_{\text{ANE}} = \alpha_{yx}\rho_{xx} + \alpha_{xx}\rho_{yx}.$$

Here, α_{xx} is the longitudinal thermoelectric constant, and α_{yx} is the transverse thermoelectric constant. The terms $\alpha_{yx}\rho_{xx}$ and $\alpha_{xx}\rho_{yx}$ correspond to S_1 and S_2 , respectively. All parameters can be determined from ρ_{xx} , ρ_{yx} , S_{xx} and S_{ANE} . S_1 represents an intrinsic mechanism where the transverse electric current is generated directly from the temperature gradient, independent of the Seebeck effect. Figure 3(g) shows S_{ANE} , S_1 , and S_2 as a function of the GdCo composition. Our findings indicate that S_1 is significantly larger than S_2 , highlighting the importance of enhancing the transverse thermoelectric constant α_{yx} and the resistivity ρ_{xx} in enhancing S_{ANE} . The magnitude of α_{yx} is dramatically enhanced with slight Gd doping and slowly decreases with Gd doping as depicted in Figs. 3(h-i). $|\alpha_{yx}|$ is relatively large even as $x = 30$. The enhancement of S_{ANE} originates from the increase in ρ_{xx} and in α_{yx} .

The origin of the large $|\alpha_{yx}|$ is commonly attributed to Berry curvature, an effective magnetic field in momentum space. However, the application of Berry curvature to amorphous materials is challenging due to the absence of periodic crystal structure. Despite this, recent studies have demonstrated the influence of Berry curvature on the anomalous Hall effect⁴⁰ and the ANE²⁵ in amorphous alloys like FeGe and FeSn. Following a widely accepted approach to validate the contributions of Berry curvature to the ANE⁴¹⁻⁴², we have plotted $|\alpha_{yx}|$ against $|\sigma_{yx}|$ in Figs. 4(a-b). By assuming a high-temperature limit, we obtain a ratio of $|\alpha_{yx}/\sigma_{yx}| \sim k_B/e$, where k_B is the Boltzmann constant and e is the elementary charge. The ratio $|\alpha_{yx}/\sigma_{yx}|$ for the GdCo films is found to be as same as $k_B/2e$, mirroring those observed in topological magnets as shown in Fig. 4(a). This consistent pattern in $|\alpha_{yx}/\sigma_{yx}|$ ratios underlines the influence of the Berry curvature on the anomalous Hall effect and ANE in GdCo films. When comparing with the crystalline GdCo₅, which shares the same crystal structure as the SmCo₅ alloy, the $|\alpha_{yx}/\sigma_{yx}|$ values for amorphous GdCo films are slightly lower than those calculated for GdCo₅ using first-principles calculations⁴⁷. This observation is reminiscent of the comparison between amorphous FeSn alloys and their crystalline counterparts, Fe₃Sn and Fe₃Sn₂, suggesting that the short-range order present in GdCo₅ also persists even in the amorphous GdCo alloys.

Sensitivity in evaluating materials for ANE-based HFS

We examined the composition dependence of the sensitivity, the ANE electric field per heat flux density. Figure 5(a) shows the schematic diagram of the measurement setup for the sensitivity. In Fig. 5(b), the detected voltage is plotted as a function of an

external magnetic field for $x = 11.1$ at room temperature. Note that the voltage at zero-magnetic field is as same as that under the high magnetic field because the GdCo films have in-plane magnetic anisotropy. Figure 5(c) illustrates the relationship between the ANE electric field E and the heat flux density j . E is completely proportional to j and its slope corresponds to the sensitivity of the material for an HFS application. Figure 5(d) shows the composition-dependent behavior of the sensitivity E/j in GdCo films. The dependency of E/j is reminiscent of that of S_{ANE} . For anisotropic materials, S_{ANE} depends on the directions of the external magnetic field and temperature gradient. However, in isotropic materials like amorphous, polycrystalline, and cubic materials, S_{ANE} is setup-independent. The similarity between E/j and S_{ANE} is reasonable owing to their linear relation ($E/j = S_{\text{ANE}}/\kappa$). In contrast, the remarked increase appears with Gd doping in the low doping region, compared with S_{ANE} . The increase is related to the suppression of the thermal conductivity. The magnitude of E/j peaks at $0.23 \mu\text{mA}^{-1}$ at $x = 23.7$, comparable to Co_2MnGa ²⁸, as shown in Figure 5(e). Although S_{ANE} in GdCo($x = 23.7$) is much smaller than $6 \mu\text{VK}^{-1}$ in Co_2MnGa , its E/j value is about the same as that of Co_2MnGa ($0.22 \mu\text{mA}^{-1}$) owing to the high thermal conductivity of $23 \text{ Wm}^{-1}\text{K}^{-1}$ in bulk Co_2MnGa ¹².

Thermal conductivity in ultrathin films

Here, we consider thermal conductivity in the GdCo films. There is no method for measuring thermal conductivity in an ultrathin metallic film in the direction perpendicular to the film. We assume the GdCo film is isotropic, indicating S_{ANE} is as same as the transverse Seebeck coefficient under the application of the in-plane magnetic field and the temperature gradient perpendicular to the films. κ is derived by $S_{\text{ANE}}/(E/j)$. Figure 5(f) depicts the composition dependence of the thermal conductivity κ . The thermal conductivity significantly decreases with Gd doping and reaches $5 \text{ Wm}^{-1}\text{K}^{-1}$, which is quite similar to $4.6\text{-}5.5 \text{ Wm}^{-1}\text{K}^{-1}$ in $\text{Gd}_{21}\text{Fe}_{72}\text{Co}_7$ and $\text{Tb}_{21}\text{Fe}_{73}\text{Co}_6$ films in the previous report³⁵. Thermal conductivity is comprised of contributions from conduction electrons, phonons, and magnons. Given the typically negligible contribution of magnon thermal conductivity, we focus on the other two. Applying the Wiedemann–Franz law and assuming that the resistivity along the z -direction, ρ_{zz} , is the same as ρ_{xx} , we calculate the electron thermal conductivity, κ_{ele} , using the equation:

$$\kappa_{\text{ele}} = LT\sigma_{zz},$$

where L is Lorentz number ($2.44 \times 10^{-8} \text{ W}\Omega\text{K}^{-2}$), T is the temperature, and $\sigma_{zz} = \rho_{xx}^{-1}$. Since the total thermal conductivity κ consists of κ_{ele} and the phonon thermal

conductivity κ_{pho} , we determined κ_{pho} as $\kappa - \kappa_{\text{ele}}$ as shown in Figure 5(g). The significant reduction in κ aligns closely with κ_{ele} , revealing that the remarked increase in the sensitivity E/j in the low doping region is closely related to the enhanced resistivity ρ_{xx} in Fig. 3(a). Meanwhile, the phonon thermal conductivity remains sufficiently low due to the amorphous nature of the materials. Therefore, enhancing the resistivity is crucial to obtaining higher sensitivity in GdCo.

Comparison of other materials

Finally, let us compare the characteristics of GdCo with other materials. The GdCo alloys have the sensitivity $|E/j|$ of $0.20 \mu\text{mA}^{-1}$ at a wide composition range around the MCP. Although this value is comparable to $0.22 \mu\text{mA}^{-1}$ in Co_2MnGa ²⁸, $0.20 \mu\text{mA}^{-1}$ in $\text{Fe}_{81}\text{Al}_{19}$ ¹, and $0.18 \mu\text{mA}^{-1}$ in $\text{Sm}_{20}\text{Co}_{80}$ ²⁹. A distinguishing feature of GdCo alloys is their bipolarity in E/j , which allows for a thermopile structure composed exclusively of GdCo pairs. Figure 6(a) shows the summary of the reported E/j , revealing only the Re-rich GdCo has negative giant sensitivity. Co_2MnGa , $\text{Fe}_{81}\text{Al}_{19}$, $\text{Sm}_{20}\text{Co}_{80}$, and $\text{Fe}_{79}\text{Ga}_{21}$ exhibit only positive E/j polarity and therefore require a different material to complete the thermopile structure. Consequently, the bipolar sensitivity of such thermopile structures, defined as $(E/j)_+ - (E/j)_-$, is effectively halved compared to those in our study, as illustrated in Figure 6(b), where $(E/j)_{+(-)}$ represents E/j in materials with $S_{\text{ANE}} > 0 (< 0)$. For HFS applications, which necessitate two materials with similar S_{xx} but larger S_{ANE} , the properties of GdCo are particularly advantageous. While Tanaka et al. achieved this using $\text{Fe}_{79}\text{Ga}_{21}$ and $\text{Fe}_{79}\text{Ga}_{21}/\text{Ni}_{10}\text{Cu}_{90}$ ³⁰, GdCo alloys offer a simpler solution by utilizing TM-rich and RE-rich compositions near the MCP. Additionally, GdCo alloys are versatile in terms of substrate compatibility; they can be deposited on any substrate at room temperature, enhancing their practical applicability. Furthermore, the transport properties of GdCo are remarkably similar to those in TbCo. Doping Tb into GdCo alloys could potentially induce a suitable magnetic anisotropy, adding another functionality to these materials.

Our findings give a guideline to obtain higher sensitivity in GdCo alloys, indicating the importance of an increase in resistivity. Since S_{ANE} is mainly attributed to the intrinsic conversion, S_{ANE} is roughly proportional to ρ_{xx} . Additionally, κ is suppressed by the increase in resistivity because the phonon thermal conductivity remains sufficiently low due to the amorphous nature. Therefore, the sensitivity E/j is roughly represented as $(\alpha_{yx}/LT)\rho_{xx}^2$ and increases with the square of the resistivity. Doping slight impurity elements into GdCo alloys may exhibit a significant enhancement of the sensitivity.

Conclusion

Our comprehensive study on the ANE in ferrimagnetic GdCo alloy films has yielded significant insights. Our results reveal that doping Gd into the alloy significantly enhances the sensitivity. Remarkably, the magnitude of the sensitivity peaks at $0.20 \mu\text{mA}^{-1}$ over a broad composition range, including the MCP, where a notable change in polarity is observed. The maximum value of $0.23 \mu\text{mA}^{-1}$ at $x = 23.7$ is comparable to the highest sensitivity found in Co_2MnGa . Additionally, the observed bipolarity of the high sensitivity is particularly advantageous for a thermopile structure. Twice sensitivity can be obtained by using the TM- and Re-rich materials, compared with the previous studies. The composition dependence of S_{ANE} suggests that the high sensitivity originates from the coexistence of a relatively large S_{ANE} (over $1.0 \mu\text{VK}^{-1}$) and low thermal conductivity (less than $5 \text{Wm}^{-1}\text{K}^{-1}$) across a wide composition range, including the MCP. Moreover, our comprehensive analysis suggests that the large S_{ANE} is attributed to Berry curvature despite its amorphous nature. GdCo alloys demonstrate an ability to be deposited on any substrate and possess a small longitudinal Seebeck coefficient. These are attributed to underscore the potential of GdCo films for use in ANE-based HFS applications.

Methods

Sample preparation

The sample structure is $\text{Si}_3\text{N}_4(10 \text{ nm}) / \text{Gd}_x\text{Co}_{100-x}(20 \text{ nm}) / \text{Si}_3\text{N}_4(3 \text{ nm})$, which was deposited on both two SiO_2 glass substrates and a Si substrate with a thermally oxidized layer using magnetron rf and dc sputtering techniques at room temperature. The base pressure in the chamber is less than 1×10^{-5} Pa. The Si_3N_4 layers act as a protection layer from the oxidation of GdCo films. For one of the glass samples, a Hall bar structure was formed using a metal mask, as depicted in Fig. 2(a). For the other glass samples and the Si-substrate sample, the films were not patterned. The GdCo alloys, varying in Gd composition from 0 to 35, were created through a co-sputtering method with Gd and Co cathodes. Gd(99.9%) and Co(99.9%) targets were purchased from Chemiston Co. The compositions of these alloys were verified via energy-dispersive X-ray spectroscopy.

Measurement method for thermal-electric transport properties

The transverse Seebeck coefficient, S_{ANE} , was measured under conditions of a perpendicular magnetic field and an in-plane thermal gradient, using the Hall bar samples as shown in Fig. 2(a). The temperature gradient was controlled using a heater and

monitored with a T-type thermocouple (copper-constantan) attached to the sample holders. While there was a minor difference between the thermocouple-measured temperature gradient and the actual gradient within the sample, this discrepancy was calibrated using thermography. To ensure the accuracy of our measurement setup, we also measured the transverse Seebeck coefficient in a polycrystalline Py film produced by magnetron sputtering, obtaining a value of $+0.53 \mu\text{VK}^{-1}$, consistent with previous findings.⁴⁸ The polarity of S_{ANE} , as defined in Fig. 2(a), aligns with established conventions: S_{ANE} is positive (>0) in materials such as Co, Ni, and Py, and negative (<0) in Fe. Additionally, the longitudinal Seebeck coefficient, electrical resistivity, and Hall resistivity were measured using the same sample, with the setups illustrated in Figs. 3(a-c). The four-terminal method was employed for electrical resistivity measurements.

Measurement method for sensitivity

The sensitivity of a material for an HFS, E/j , was measured under the condition of an in-plane magnetic field using the unpatterned samples prepared on glass substrates as shown in Fig. 5(a). The sample was sandwiched between Cu blocks and heat was applied to the sample in the direction perpendicular to the film by a heater. The heat flow through the sample is monitored by a commercialized HFS connected to the sample in series. To reduce a contact thermal resistance, we used thermal greases ($8.3 \text{ Wm}^{-1}\text{K}^{-1}$) for a CPU device in a PC. To calibrate the accuracy of our measurement setup, we also measured E/j in a Py film produced by magnetron sputtering, obtaining values of $+0.017 - +0.018 \mu\text{mA}^{-1}$, consistent with S_{ANE}/κ in the previous reports⁴⁸⁻⁴⁹. The polarity of E/j aligns with established conventions: E/j is positive (negative) as $S_{\text{ANE}} > 0$ (< 0).

Data Availability

The data that support the findings of this study are available from the corresponding author upon reasonable request.

References

1. Zhou, W. and Sakuraba, Y. Heat flux sensing by anomalous Nernst effect in Fe–Al thin films on a flexible substrate. *Applied Physics Express* **13**, 043001 (2020).
2. Nernst, W. Ueber die electromotorischen Kräfte, welche durch den Magnetismus in von einem Wärmestrome durchflossenen Metallplatten geweckt werden. *Annalen der Physik* **267**, 760 (1887).

3. Sakuraba, Y. et al., Anomalous Nernst Effect in L1₀-FePt/MnGa Thermopiles for New Thermoelectric Applications. *Applied Physics Express* **6**, 033003 (2013).
4. Sakuraba, Y. Potential of thermoelectric power generation using anomalous Nernst effect in magnetic materials. *Scripta Materialia* **111**, 32 (2016).
5. Ramos, R. et al., Anomalous Nernst effect of Fe₃O₄ single crystal. *Phys. Rev. B* **90**, 054422 (2014).
6. Hasegawa, K. et al., Material dependence of anomalous Nernst effect in perpendicularly magnetized ordered-alloy thin films. *Appl. Phys. Lett.* **106**, 252405 (2015).
7. Uchida, K.-i. et al., Enhancement of anomalous Nernst effects in metallic multilayers free from proximity-induced magnetism. *Phys. Rev. B* **92**, 094414 (2015).
8. Ando, R. Komine, T. and Hasegawa, Y. Anomalous Nernst Effect of Perpendicularly Magnetic Anisotropy TbFeCo Thin Films. *J. Electron. Mater.* **45**, 3570 (2016).
9. Isogami, S. Takanashi K. and Mizuguchi, M. Dependence of anomalous Nernst effect on crystal orientation in highly ordered γ' -Fe₄N films with anti-perovskite structure. *Appl. Phys. Express* **10**, 073005 (2017).
10. Chuang, T. C. Su, P. L. Wu, P. H. and Huang, S. Y. Enhancement of the anomalous Nernst effect in ferromagnetic thin films. *Phys. Rev. B* **96**, 174406 (2017).
11. Ando, R. and Komine, T. Geometrical contribution to the anomalous Nernst effect in TbFeCo thin films. *AIP Advances* **8**, 056326 (2018).
12. Ikhlas, M. et al., Large anomalous Nernst effect at room temperature in a chiral antiferromagnet. *Nature Physics* **13**, 1085 (2017).
13. Sakai, A. et al., Giant anomalous Nernst effect and quantum-critical scaling in a ferromagnetic semimetal. *Nature Physics* **14**, 1119 (2018).
14. Guin, S. N. et al., Anomalous Nernst effect beyond the magnetization scaling relation in the ferromagnetic Heusler compound Co₂MnGa. *NPG Asia Materials* **11**, 16 (2019).
15. Sumida, K. et al., Spin-polarized Weyl cones and giant anomalous Nernst effect in ferromagnetic Heusler films. *Communications Materials* **1**, 89 (2020).
16. Nakayama, H. et al., Mechanism of strong enhancement of anomalous Nernst effect in Fe by Ga substitution. *Phys. Rev. Materials* **3**, 114412 (2019).

17. Sakai, A. et al., Iron-based binary ferromagnets for transverse thermoelectric conversion. *Nature* **581**, 53 (2020).
18. Sakuraba, Y. Hyodo, K. Sakuma, A. and Mitani, S. Giant anomalous Nernst effect in the $\text{Co}_2\text{MnAl}_{1-x}\text{Si}_x$ Heusler alloy induced by Fermi level tuning and atomic ordering *Phys. Rev. B* **101**, 134407 (2020).
19. Yang, H. et al., Giant anomalous Nernst effect in the magnetic Weyl semimetal $\text{Co}_3\text{Sn}_2\text{S}_2$. *Phys. Rev. Materials* **4**, 024202 (2020).
20. Noguchi S. et al., *Nature Physics* Bipolarity of large anomalous Nernst effect in Weyl magnet-based alloy films. **20**, 254-260 (2024).
21. Chen, T. et al., Anomalous transport due to Weyl fermions in the chiral antiferromagnets Mn_3X , X = Sn, Ge. *Nature Communications* **12**, 572 (2021).
22. Asaba, T. et al., Colossal anomalous Nernst effect in a correlated noncentrosymmetric kagome ferromagnet. *Science Advances* **7**, eabf1467 (2021).
23. Khadka, D. et al., Anomalous Hall and Nernst effects in epitaxial films of topological kagome magnet Fe_3Sn_2 . *Phys. Rev. Materials* **4**, 084203 (2020).
24. Chen, T. et al., Large anomalous Nernst effect and nodal plane in an iron-based kagome ferromagnet. *Science Advances* **8**, eabk1480 (2022).
25. Fujiwara, K. et al., Berry curvature contributions of kagome-lattice fragments in amorphous Fe–Sn thin films. *Nature Communications* **14**, 3399 (2023).
26. Roychowdhury, S. et al., Large Room Temperature Anomalous Transverse Thermoelectric Effect in Kagome Antiferromagnet YMn_6Sn_6 . *Adv. Mater.* **34**, 2201350 (2022).
27. Pan, Y. et al., Giant anomalous Nernst signal in the antiferromagnet YbMnBi_2 . *Nature Materials* **21**, 203–209 (2022)
28. Uchida, K.-i. Zhou, W. and Sakuraba, Y. Transverse thermoelectric generation using magnetic materials. *Appl. Phys. Lett.* **118**, 140504 (2021).
29. Modak, R. et al., Sm-Co-based amorphous alloy films for zero-field operation of transverse thermoelectric generation. *Sci. Technol. Adv. Mater.* **23**, 767 (2022).
30. Tanaka, H. et al., Roll-to-Roll Printing of Anomalous Nernst Thermopile for Direct Sensing of Perpendicular Heat Flux. *Advanced Materials* **35**, 2303416 (2023).
31. Yagmur, A. Sumi, S. Awano, H. and Tanabe, K. Large Inverse Spin Hall Effect in Co-Tb Alloys due to Spin Seebeck Effect. *Phys. Rev. Appl.* **14**, 064025 (2020).

32. Fukuda, S. Awano, H. and Tanabe, K. Observation of spin-motive force in ferrimagnetic GdFeCo alloy films. *Appl. Phys. Lett.* **116**, 102402 (2020).
33. Yagmur, A. Sumi, S. Awano, H. and Tanabe, K. Magnetization-dependent inverse spin Hall effect in compensated ferrimagnet TbCo alloys. *Physical Review B* **103**, 214408 (2021).
34. Kuno, S. Deguchi, S. Sumi, S. Awano, H. and Tanabe, K. Estimation of TbCo composition from a local-minimum-energy magnetic state taken by magneto-optical-Kerr-effect microscope by using machine learning. *APL Machine Learning* **1**, 046111 (2023).
35. Hopkins, P. E. Ding M. and Poon, J. Contributions of electron and phonon transport to the thermal conductivity of GdFeCo and TbFeCo amorphous rare-earth transition-metal alloys. *J. Appl. Phys.* **111**, 103533 (2012).
36. Seki, T. Miura, A. Uchida, K.-i. Kubota, T. and Takanashi, K. Anomalous Ettingshausen effect in ferrimagnetic Co–Gd *Appl. Phys. Express* **12**, 023006 (2019).
37. Liu, R. et al., Anomalous Nernst effect in compensated ferrimagnetic Co_xGd_{1-x} films. *Appl. Phys. Lett.* **122**, 022406 (2023).
38. Kobayashi, Y. Kasatani, Y. Yoshikawa, H. and Tsukamoto, A. Effect of anomalous Hall resistivity on anomalous Nernst coefficient in amorphous GdFe ferrimagnetic alloy thin film. *T. Magn. Soc. Jpn.* **7**, 34 (2023) in Japanese.
39. Odagiri, M. et al., Coexistence of large anomalous Nernst effect and large coercive force in amorphous ferrimagnetic TbCo alloy films. *Applied Physics Letters* **124**, 142403 (2024).
40. Bouma, D. S. et al., Itinerant ferromagnetism and intrinsic anomalous Hall effect in amorphous iron-germanium. *Phys. Rev. B* **101**, 014402 (2020).
41. Xu, L. et al., Anomalous transverse response of Co₂MnGa and universality of the room-temperature $\alpha^{A_{ij}}/\sigma^{A_{ij}}$ ratio across topological magnets. *Phys. Rev. B* **101**, 180404(R) (2020).
42. Ding, L. et al., Intrinsic Anomalous Nernst Effect Amplified by Disorder in a Half-Metallic Semimetal. *Phys. Rev. X* **9**, 041061 (2019).
43. Miyasato, T. et al., Crossover Behavior of the Anomalous Hall Effect and Anomalous Nernst Effect in Itinerant Ferromagnets. *Phys. Rev. Lett.* **99**, 086602 (2007).
44. Xu, L. et al., Finite-temperature violation of the anomalous transverse Wiedemann-Franz law. *Science Advances* **6**, eaaz3522 (2020).

45. Zhang, H. Xu, C. Q. and Ke, X. Topological Nernst effect, anomalous Nernst effect, and anomalous thermal Hall effect in the Dirac semimetal Fe_3Sn_2 . *Phys. Rev. B* **103**, L201101 (2021).
46. Guin, S. N. et al., Zero-Field Nernst Effect in a Ferromagnetic Kagome-Lattice Weyl-Semimetal $\text{Co}_3\text{Sn}_2\text{S}_2$. *Advanced Materials* **31**, 1806622 (2019).
47. Miura, A. et al., Observation of anomalous Ettingshausen effect and large transverse thermoelectric conductivity in permanent magnets. *Appl. Phys. Lett.* **115**, 222403 (2019).
48. Yamazaki, T. et al., Thickness dependence of anomalous Hall and Nernst effects in Ni-Fe thin films. *Phys. Rev. B* **105**, 214416 (2022).
49. Kikkawa, T. et al., Separation of longitudinal spin Seebeck effect from anomalous Nernst effect: Determination of origin of transverse thermoelectric voltage in metal/insulator junctions. *Phys. Rev. B* **88**, 214403 (2013).

Acknowledgements

This work was mainly supported by the Paloma Environmental Technology Development Foundation.

Author information

Authors and Affiliations

Toyota Technological Institute, Nagoya, 468-8511, Japan

M. Odagiri, H. Imaeda, A. Yagmur, S. Sumi, H. Awano, K. Tanabe

University of Leeds, Leeds, LS2 9JT, UK

A. Yagmur

Graduate School and Faculty of Information Science and Electrical Engineering, Kyushu University, Fukuoka, 819-0395, Japan

Y. Kurokawa

Contributions

K.T. conceived the project. M.O. prepared the samples used in this study. M.O. mainly performed measurements and H.I., A.Y., Y.K., S.S., H.A., and K.T. supported her. M.O. and K.T. carried out the analysis. K.T. wrote the paper. All authors discussed the results and reviewed the paper.

Corresponding authors

Correspondence to Kenji Tanabe.

Ethics declarations

Competing interests

The authors declare no competing financial or non-financial interests.

Caption

Figure 1

Schematic diagram of a transverse thermopile device based on ANE. The blue and orange wires indicate magnetic materials with positive and negative S_{ANE} , respectively.

Figure 2

(a-b) Schematic illustrations of setups for measuring S_{ANE} . (c) ANE voltage as functions of a magnetic field and temperature difference as $x = 15.5$ at room temperature. (d) Relationship between the electric field and temperature gradient as $x = 15.5$. The blue line indicates a linear fitting line and its slope corresponds to S_{ANE} . (e) Transverse Seebeck coefficient as a function of GdCo composition. The blue triangle data were referred from the previous report³⁹. The green dotted curves are guides to the eye.

Figure 3

(a-c) Schematic illustrations of setups for measuring electrical resistivity(a), Hall resistivity(b), and longitudinal Seebeck coefficient(c). (d-f) ρ_{xx} (d), ρ_{yx} (e), and S_{xx} (f) as a function of GdCo composition at room temperature. All the parameters were measured by using the same sample. The four-terminal method was used in the resistance measurement. The blue triangle data were referred from the previous report³⁹. (g) S_{ANE} , S_1 , and S_2 as a function of GdCo composition. S_2 is derived by $S_{xx}\rho_{yx}/\rho_{xx}$ from Figs. 3(d-f). S_1 is derived by $S_{ANE} - S_2$. (h-i) α_{yx} (h) and its magnitude(i) as a function of GdCo composition.

Figure 4

(a) Summary of the relationship between $|\alpha_{yx}|$ and $|\sigma_{xy}|$ in topological magnets. $\sigma_{xy} = \rho_{yx}/(\rho_{xx}^2 + \rho_{yx}^2)$. La_{0.3}Sr_{0.7}CoO₃, Mn₃Sn, Mn₃Ge, Fe₃Sn₂, Fe_{0.7}Ga_{0.3}, Fe₃Sn, Co₃Sn₂S₂, and Co₂MnGa indicate La_{0.3}Sr_{0.7}CoO₃ cryst-bulk⁴⁶, Mn₃Sn cryst-bulk¹², Mn₃Ge cryst-bulk⁴⁷, Fe₃Sn₂ cryst-bulk⁴⁸, Fe_{0.7}Ga_{0.3} cryst-film¹⁶, Fe₃Sn cryst-bulk²⁴, Co₃Sn₂S₂ cryst-bulk^{45, 49}, and Co₂MnGa cryst-bulk¹³, respectively. The blue triangle data were referred from the previous report³⁹, (b) Comparison of the relationship between $|\alpha_{yx}|$ and $|\sigma_{yx}|$ in GdCo alloys with single-crystalline GdCo₅ alloy. The data in GdCo₅ was referred from the supplementary information in the previous report⁴⁷.

Figure 5

(a) Schematic illustrations of setups for measuring E/j . The directions of a magnetic field and heat flux in this setup differ from those in Figs. 2 (c-d). (b) ANE voltage as functions of a magnetic field and a heat flux density as $x = 11.1$ at room temperature. (c) ANE electric field as a function of a heat flux density as $x = 11.1$. The blue line indicates a linear fitting line. (d-e) E/j (d) and its magnitude(e) as a function of GdCo composition, x . (f) Thermal conductivity as a function of GdCo composition, x . The thermal conductivity κ is derived by $S_{\text{ANE}}/(E/j)$. Here, we assumed that S_{ANE} is isotropic. The blue dotted line corresponds to the thermal conductivity in $\text{Tb}_{21}\text{Fe}_{73}\text{Co}_6$ ³⁵. (g) Total, electron, and phonon thermal conductivities as a function of GdCo composition, x . electron thermal conductivity is derived by $LT\sigma_{xx}$, where L is the Lorentz number and σ_{xx} is the longitudinal electrical conductivity along the in-plane direction. Here, we assumed that σ_{xx} is isotropic. The phonon thermal conductivity is the difference between the total and electron thermal conductivities.

Figure 6

(a) Summary of sensitivity of heat flux densities. FeAl, SmCo, FeGa, and Co_2MnGa indicate a $\text{Fe}_{81}\text{Al}_{19}$ film¹, a Co_2MnGa film²⁷, an $\text{Sm}_{20}\text{Co}_{80}$ film²⁸, and a $\text{Fe}_{79}\text{Ga}_{21}$ film²⁹, respectively. GdCo(TM) and GdCo(RE) correspond to a $\text{Gd}_{15.5}\text{Co}_{84.5}$ film and a $\text{Gd}_{23.7}\text{Co}_{76.3}$ film in this study, respectively. Although E/j is not shown in previous reports^{1, 27-29}, it was estimated from the reported sensor sensitivity V/j and the sample shape, (b) Summary of sensitivity of thermopile for HFS. FeAl/Au, $\text{Co}_2\text{MnGa}/\text{Au}$, SmCo/Au, and FeGa/CuNi indicate a $\text{Fe}_{81}\text{Al}_{19}\text{-Au}$ thermopile¹, a $\text{Co}_2\text{MnGa}\text{-Au}$ thermopile²⁷, a $\text{Sm}_{20}\text{Co}_{80}\text{-Au}$ thermopile²⁸, and a $\text{Fe}_{81}\text{Ga}_{19}\text{-Fe}_{81}\text{Ga}_{19}/\text{Cu}_{90}\text{Ni}_{10}$ thermopile²⁹, respectively. GdCo/GoCo corresponds to the case of a $\text{Gd}_{15.5}\text{Co}_{84.5}\text{-Gd}_{23.7}\text{Co}_{76.3}$ thermopile device.

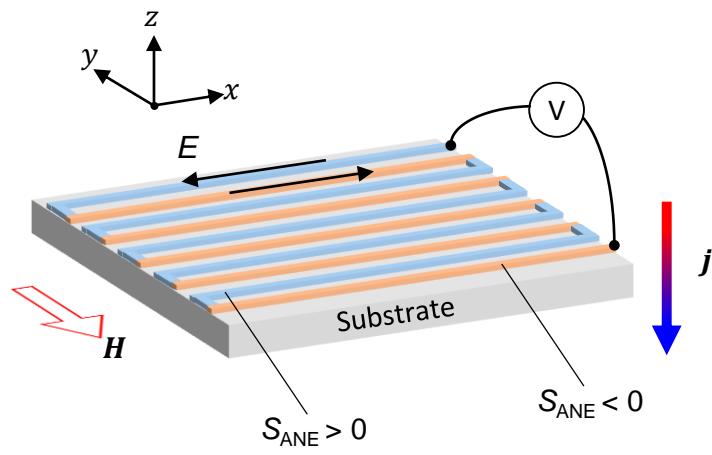


Figure 1

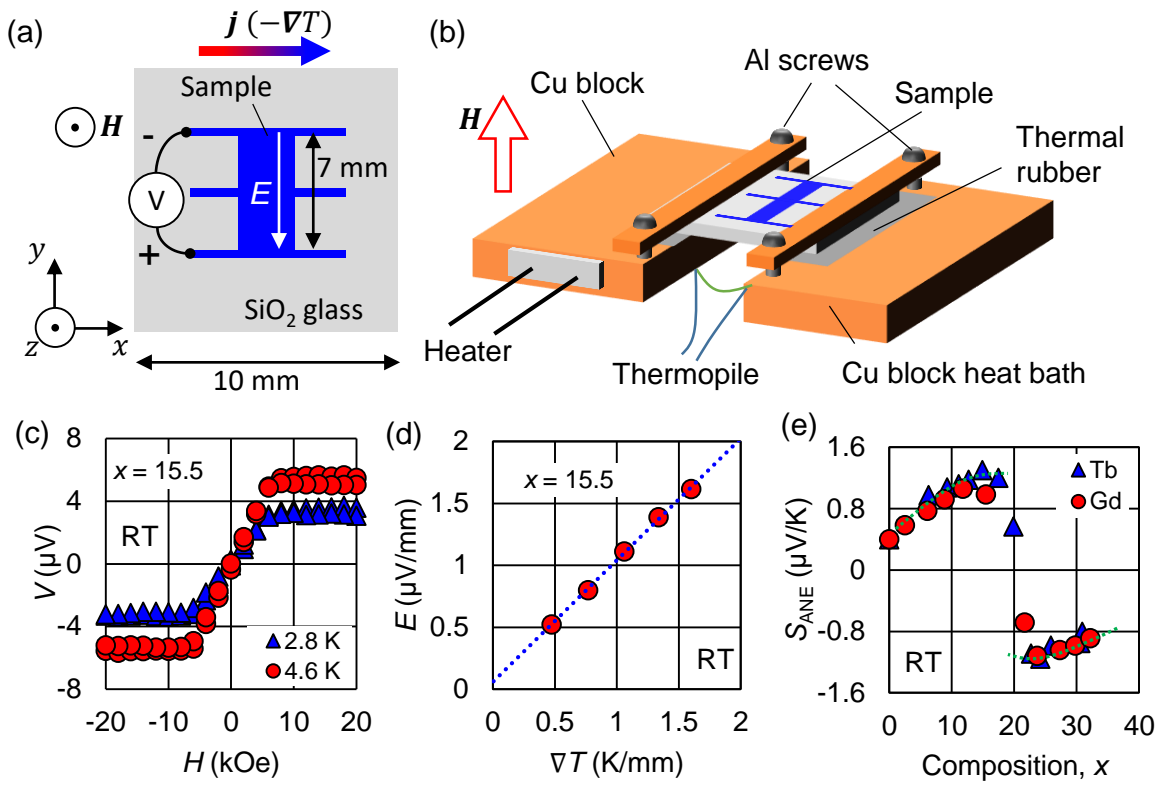


Figure 2

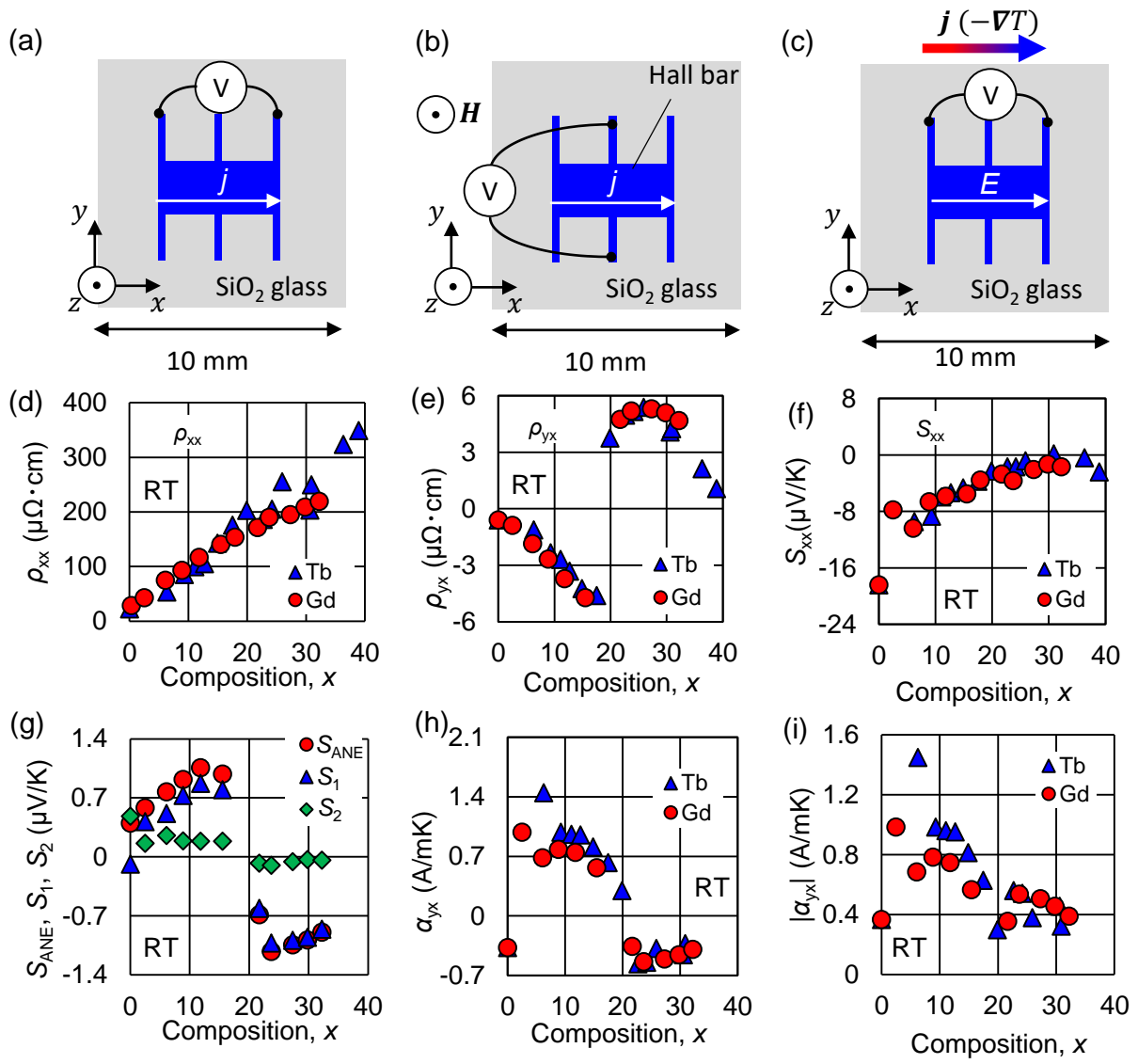


Figure 3

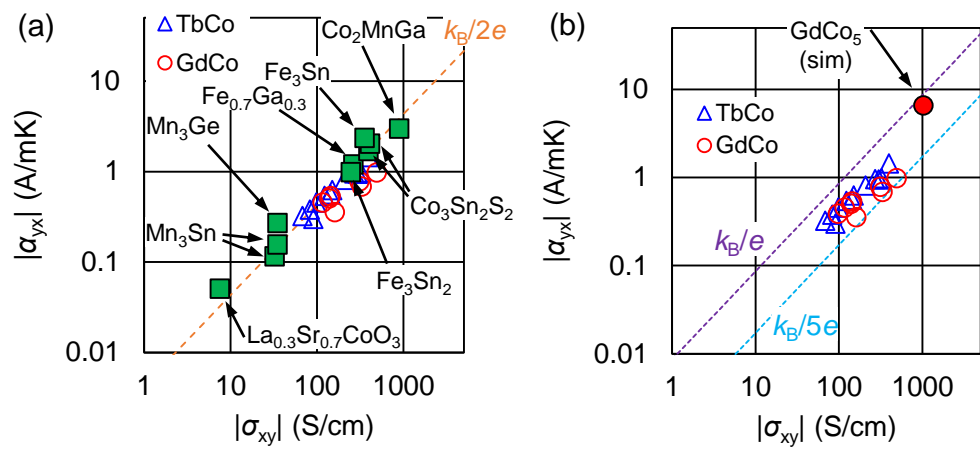


Figure 4

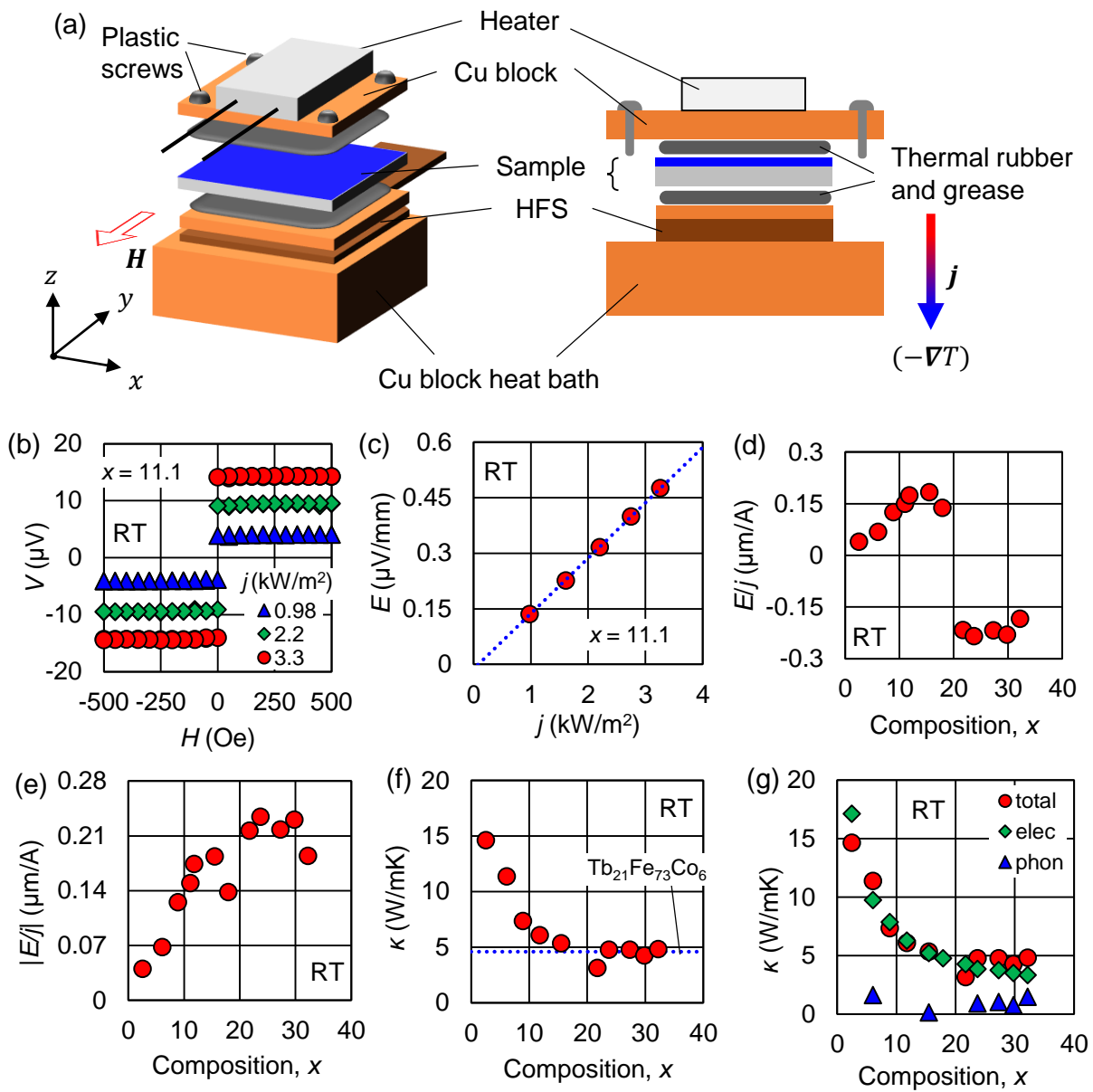


Figure 5

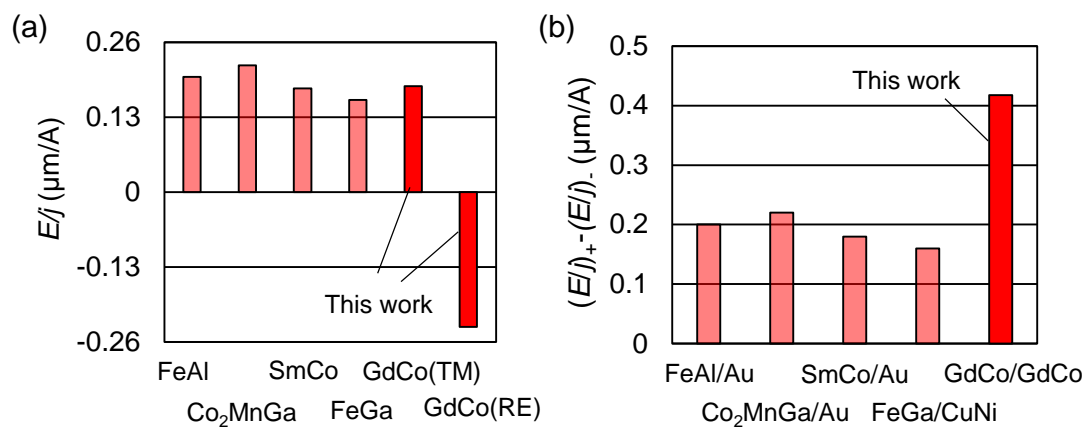


Figure 6